



Defective heterojunctions in CO₂ photoreduction: Enabling ultrafast interfacial charge transfer and selective methanation



Shuwen Cheng ^{a,b,1}, Zhehao Sun ^{c,1}, Kang Hui Lim ^b, Kaili Liu ^c, Ary Anggara Wibowo ^d, Tao Du ^a, Liying Liu ^a, Hieu T. Nguyen ^d, Gang Kevin Li ^{e,*}, Zongyou Yin ^{c,*}, Sibudjing Kawi ^{b,*}

^a School of Metallurgy, Northeastern University, Shenyang 110819, PR China

^b Department of Chemical and Biomolecular Engineering, National University of Singapore, Singapore 119260, Singapore

^c Research School of Chemistry, Australian National University, Canberra, ACT 2601, Australia

^d School of Engineering, Australian National University, Canberra, ACT 2601, Australia

^e Department of Chemical Engineering, The University of Melbourne, Melbourne, VIC 3010, Australia

ARTICLE INFO

Keywords:

Defects
Heterojunction
CO₂ photoreduction
Ultrafast charge transfer channels

ABSTRACT

This study achieved the goal of enhancing photocatalytic methane production and selectivity by constructing a *S*-scheme heterojunction of TiO₂/g-C₃N₄ followed by conducting a mild-temperature hydrogen reduction to remove hydroxyl groups from the catalyst surface, thereby generating rich vacancies-related active sites. The rate of CO₂ photoreduction to CH₄ under pure water from the H₂-Ti-CN sample is around 27.4 μmol g⁻¹ h⁻¹ with 93.6% selectivity, which is 39.1-fold and 5.59-fold that of pristine g-C₃N₄ and TiO₂, respectively. In addition, the DFT calculation indicates that the vacancies created via hydrogen reduction-mediated heterojunctions effectively tune the energy barrier, resulting in a decrease in the production of the two-electron product CO and concurrently improves the selectivity of the eight-electron reaction. The significantly enhanced photocatalytic performance is ascribed to defects fostering ultrafast charge carrier transfer channels and facilitating the transfer of light-excited charges to the surface, thereby enhancing its high redox capabilities in catalytic reactions.

1. Introduction

Photocatalytic reduction of carbon dioxide (CO₂) into renewable energy sources has emerged as a promising approach for addressing the global challenges of greenhouse gas emissions and energy sustainability [1–3]. Titanium dioxide (TiO₂), a widely studied and well-known semiconductor, possesses excellent photochemical stability and a suitable bandgap for solar light absorption [4,5]. However, its intrinsic limitations, such as a wide bandgap and fast recombination of photo-generated electron-hole pairs, hinder its efficiency in CO₂ conversion [6]. On the other hand, g-C₃N₄, an emerging two-dimensional carbon-based material, exhibits desirable properties like excellent visible light absorption and moderate bandgap, making it a promising candidate for photocatalytic applications [7–9].

Photocatalytic CO₂ to methane (CH₄) conversion is an eight-electron transfer process, which makes it challenging for most photocatalysts to efficiently carry out this reaction [10–14]. Many conventional photocatalysts have limitations in terms of their band structures, surface

properties, and charge carrier dynamics, which can hinder the efficient transfer and utilization of multiple electrons [15–18]. The relatively high energy barriers and the potential for electron-hole recombination further increase the difficulty of achieving effective CO₂ to CH₄ conversion [19,20]. To overcome these challenges, extensive research efforts are focused on developing advanced photocatalytic materials with enhanced capabilities. Constructing a heterojunction structure is one of the widely used strategies for enhancing the efficiency of photocatalytic CO₂ to CH₄ conversion [21,22]. Generally, heterojunctions facilitate efficient charge separation and transfer, broaden the absorption range of the photocatalyst, improve charge transport, and even the creation of new active sites for CO₂ photoreduction [23–25]. Research on TiO₂/g-C₃N₄ heterojunctions has emerged recently in photocatalysis [26–28], including degradation [28], antibiotic removal [29], levofloxacin removal [30], CO₂ reduction into CO and CH₄ [27,31]. However, the multi-electron transfer and high energy barrier associated with the conversion of CO₂ to CH₄ typically result in CO being the predominant product, thus limiting the selectivity towards CH₄ [32]. Some

* Corresponding authors.

E-mail addresses: li.g@unimelb.edu.au (G.K. Li), zongyou.yin@anu.edu.au (Z. Yin), chekawis@nus.edu.sg (S. Kawi).

¹ These authors contributed equally.

research works have improved the methane yield and selectivity of heterojunction photocatalysts by doping or adding co-catalysts such as noble metals [21,33], which undoubtedly increases the cost of photocatalytic reactions, making this energy-saving and environmentally friendly reaction unaffordable. Therefore, non-metal loaded heterojunction photocatalyst materials have emerged as promising alternatives in various applications due to their cost-effectiveness, abundant availability, and comparable or even superior performance to metal counterparts [34–36].

In this work, we investigate a S-scheme $\text{TiO}_2/\text{g-C}_3\text{N}_4$ heterojunction photocatalyst, which incorporates surface defects through hydrogen reduction treatment, for high-selectivity photoreduction of CO_2 to CH_4 in a solid-gas phase reaction without the adding of sacrificial agents. First, we prepared ultrathin, porous $\text{g-C}_3\text{N}_4$. Then, as a substrate, we combined TiO_2 nanoparticles onto it using a simple one-step hydrothermal method. Next, the heterojunction samples were subjected to a hydrogen (H_2) reduction treatment at 300 °C for 2 h, resulting in a photocatalyst with a high concentration of defects. The increase in the concentration of defects was confirmed through electron paramagnetic resonance (EPR) and ex situ/in situ X-ray photoelectron spectroscopy (XPS) spectra, which correlated with a noticeable enhancement in photocatalytic activity and selectivity with favorable stability. These defects play a crucial role in opening ultrafast charge transfer channels at the heterojunction interface. Photoluminescence (PL), time-resolved photoluminescence (TRPL), femtosecond time-resolved absorption spectroscopy (fs-TAS) and electron spin resonance (ESR) characterizations provide strong evidence for the opening of charge transfer channels and the direction of electron flow. Furthermore, density functional theory (DFT) calculations offer a detailed mechanistic analysis of the positive effect of defects on CH_4 generation.

2. Experimental section

2.1. Materials

All chemical reagents used in this work were analytical reagent grade and without further purification. Urea, titanium (IV) butoxide (TTB), and ethanol were all purchased from Sigma-Aldrich Co., Ltd. Deionized water was used throughout the whole experimental process.

2.2. Synthesis of $\text{TiO}_2/\text{g-C}_3\text{N}_4$ heterojunction

First, $\text{g-C}_3\text{N}_4$ was prepared by annealing urea at 550 °C for 2 h with a heating rate of 5 °C min⁻¹. Then, the yellow powder was obtained which is the pristine $\text{g-C}_3\text{N}_4$. For the preparation of $\text{TiO}_2/\text{g-C}_3\text{N}_4$ heterojunction, 50 mg of $\text{g-C}_3\text{N}_4$ was first dispersed in 10 mL of deionized water and sonicated for 30 min (Solution A). A certain amount of TTB solution (12.5 μL, 25 μL, 37.5 μL, and 50 μL) was added dropwise into 50 mL ethanol stirred for 10 min, and then mixed with Solution A for another 20-minute string (Solution B). Solution B was centrifuged and washed twice with ethanol, then dispersed the sample in 50 mL of water and stirred at 100 °C for 2 h. After the suspension was cooled to room temperature, centrifuged, and dried to obtain the pale-yellow samples (named as 12.5Ti-CN, 25Ti-CN, 37.5Ti-CN and 50Ti-CN according to the amount of added TTB solution respectively). The pristine TiO_2 sample was prepared by the above procedure without the addition of Solution A. All TiO_2 -related samples were annealed at 450 °C for 2 h in the air to form crystallized anatase TiO_2 .

2.3. Synthesis of $\text{H}_2\text{-TiO}_2/\text{H}_2\text{-g-C}_3\text{N}_4$ heterojunction

A schematic diagram for the preparation of $\text{H}_2\text{-Ti-CN}$ is shown in Fig. S1. The $\text{H}_2\text{-TiO}_2$, $\text{H}_2\text{-CN}$, and $\text{H}_2\text{-Ti-CN}$ samples are prepared by H_2 reduction methods at 300 °C by exposing the TiO_2 , $\text{g-C}_3\text{N}_4$ and 25Ti-CN samples to a flow of 10% H_2 /90% He mixture gas using a tubular furnace.

2.4. Material characterizations

X-ray diffraction (XRD) patterns were performed by XRD-6000 powder diffractometer, Shimadzu; Bruker, D2 PHASER. The scanning range was set up from 10° to 60° with a 2° min⁻¹ rate using a Cu K α radiation source ($\lambda = 1.5406 \text{ \AA}$). The scanning electron microscopy (SEM) images and energy dispersive X-ray (EDX) mapping analysis were conducted by 7610 Plus, JEOL on a field emission scanning electron microscopy (FESEM). High-resolution transmission electron microscope (HRTEM) images were performed by JEOL JEM-2100 F. The ex and in situ XPS and ultraviolet photoelectron spectroscopy (UPS) of the samples were carried out using a photoelectron spectrometer (ESCA-LAB250Xi, Thermo Fisher Scientific), the He I light source (21.22 eV) with a bias of 5 eV was used for UPS measurement. EPR measurement was done on a commercial BRUKE EMX spectrometer under low temperature with the following parameters: the central magnetic field is 3430 Gauss, the scan time is 15 s, the power is 1.5 mW, the modulation amplitude is 1 Gauss, the conversion time is 50 ms, and the frequency is 9.45 GHz. The fs-TAS was performed on the Femto-TA100 ultrafast transient absorption spectroscopy system. The fs-TAS were carried out under vacuum, with the sample dissolved in a glycerol-water solution (3.5 wt%). UV-vis absorption spectra were measured by Shimadzu UV-3600 UV-vis spectrophotometer. The ESR spectroscopy was measured by an A300 spectrometer from Bruker under low temperatures. Fourier transform infrared spectroscopy (FT-IR) spectrum and in situ diffuse reflectance infrared Fourier transform spectroscopy (DRIFT) were measured by the FT-IR Vertex 70 spectrometer, Bruker. Steady-state PL spectra were measured by FLS980 Fluorescence Spectrofluorometer (Edinburgh) with an excitation of 325 nm. TRPL was measured at room temperature by the Horiba iHR 320 mm spectrophotometer equipped with a compact single-photon silicon detector (PPD-900, detection range between 350 and 920 nm).

2.5. Photocatalytic activity test

The photocatalytic CO_2 reduction reaction was carried out in a gas-solid phase reaction system (PLZR-GSRS, Beijing Perfectlight, China). The reaction was conducted under light irradiation of a 300 W Xe lamp (CEL-PE300-3A, Beijing Aulight, China) while CO_2 was passed through H_2O bubbling into the reactor, without the use of any sacrificial agents. Typically, 10 mg of the sample was dispersed in 2 mL deionized water sonicated for 15 min. Then, dropped the suspension on a glass substrate, and dried at room temperature naturally to form a thin film. Subsequently, the glass substrate with the sample was placed into the Pyrex reactor connected to the gas-solid phase reaction system. Then, the Pyrex reactor was sealed, and pure CO_2 was injected for 20 min to remove air contamination. The Pyrex reactor is a double layer wall jacketed glass reactor that allows water circulation with a pump to maintain the reactor at room temperature during the reaction. At last, the Xe lamp was turned on to conduct the reaction. The photocatalytic CO_2 reduction products were analyzed by a gas chromatograph (GC-2014, Shimadzu Corp., Japan) equipped with a flame ionization detector (FID) and the thermal conductivity detector (TCD).

2.6. Electrochemistry measurement

Electrochemical properties, including photo photocurrent, electrochemical impedance spectroscopy and FRA tests, were measured via an electrochemical station (PGSTAT302N, Metrohm Autolab). Electrochemical measurements were conducted utilizing a conventional three-electrode system, with saturated Ag/AgCl electrodes as reference electrodes (RE) and graphite electrodes as counter electrodes (CE). The working electrodes were fabricated on Fluorine-doped tin oxide (FTO) glass (1 cm × 2 cm). Initially, the FTO glass was sequentially sonicated in acetone, ethanol, and water for 20 min each. Subsequently, a mixture of 10 mg of the sample and 50 μL of 5 wt% Nafion 117 solution was

dispersed in 1 mL of ethanol and sonicated for 15 min. A 300 μ L suspension was then deposited onto the FTO glass and dried for 30 min at 60 °C. The system was immersed in a 0.5 M Na₂SO₄ aqueous solution (pH=6.8) and connected to the electrochemical station for measurement.

2.7. Theoretical calculations

All the calculations are done based on DFT calculation using the Vienna ab initio simulation package (VASP) [37,38]. The theory uses the projected augmented wave method (PAW) pseudopotentials[39], and to calculate the Gibbs free energy, the generalized gradient approximation (GGA) method with Perdew–Burke–Ernzerhof (PBE)

exchange-correlation functional was employed [40]. The wave-plane cutoff energy is set to 400 eV, and the Monkhorst-Pack grid of $3 \times 3 \times 1$ k points is selected for the K point. Convergence criteria are selected as energy less than 10^{-4} eV and force less than 0.02 eV/Å. DFT-D3 method [41] is considered as van der Waals (vdW) correction. To prevent the interaction between atoms, we chose the slab model with 30 Å in the C direction. Furthermore, we performed a zero potential energy correction (ZEP) on the adsorption energy to obtain accurate free energies.

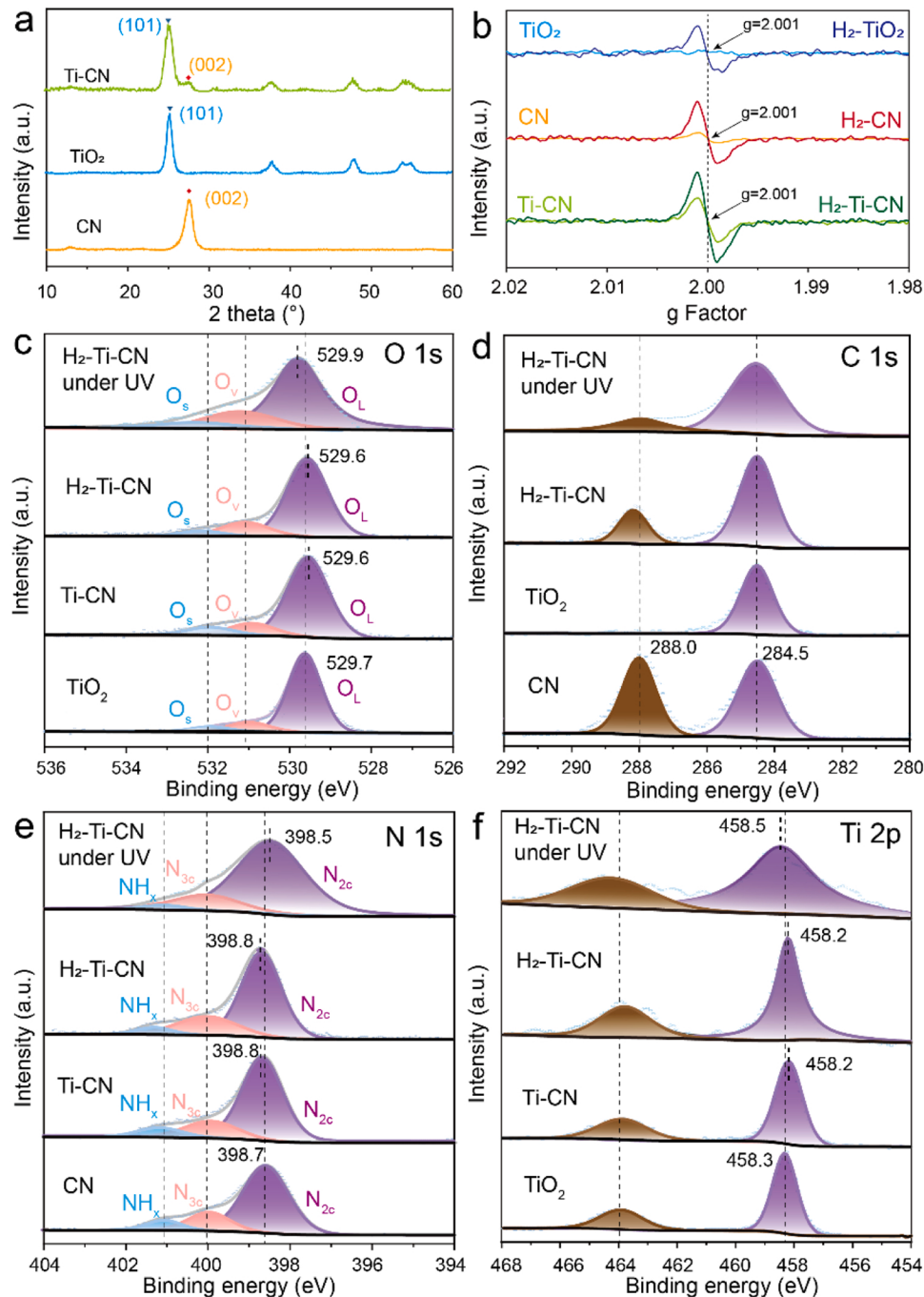


Fig. 1. (a) XRD patterns of CN, TiO₂ and Ti-CN samples. (b) EPR spectra of all the samples. Ex- situ and in-situ XPS spectra of (c) O 1s, (d) C 1s, (e) N 1s and (f) Ti 2p.

3. Results and discussion

3.1. Materials characterization

The XRD patterns of as-prepared samples are given in Fig. 1a. It can be observed that the as-synthesized TiO_2 is composed of anatase TiO_2 , with the (101) crystal plane being the main component at 24.6° . The characteristic peak of $\text{g-C}_3\text{N}_4$ is mainly observed at the (002) plane at 27.3° . Characteristic reflection peaks of anatase TiO_2 (JCPDS no. 21-1272) and $\text{g-C}_3\text{N}_4$ (JCPDS no. 87-1526) can be seen in the TiO_2 - $\text{g-C}_3\text{N}_4$ (Ti-CN) heterojunction sample. To explore the existence of vacancies before and after the H_2 reduction, the solid EPR spectra of samples were measured (Fig. 1b) [42]. The signal of TiO_2 shows slight fluctuations after H_2 reduction treatment, indicating the formation of a small number of oxygen vacancies [43]. A notable contrast is observed in CN and Ti-CN samples, that is, a significant stronger EPR resonance signal is consistently observed after their treatment with hydrogen, which can be mainly attributed to the increased concentration of N vacancies in the $\text{g-C}_3\text{N}_4$ [44]. The EPR results qualitatively show the increase in the vacancy content [45]. Simultaneously, Raman spectroscopy observed that the absorption characteristic peaks of CN-containing samples at 479, 709, and 985 cm^{-1} became broader and weaker, and there was a noticeable shift towards higher wavenumbers, as shown in Fig. S2. This phenomenon may be attributed to hydrogen treatment causing crystal defects within the CN, which strongly influences the characteristic vibrational frequencies of CN-containing samples, aligning well with EPR results [46].

The surface chemical states of the series of samples were further

investigated by the XPS technique. The O 1s peaks around 529.7, 531.1 and 532.0 eV in Fig. 1c are attributed to lattice oxygen (O_L), vacancy oxygen (O_v) and surface hydroxyl groups (O_s), respectively [47]. For the H_2 -Ti-CN sample, the proportion of O_v peak has increased, attributed to the increase of oxygen vacancy in the H_2 -Ti-CN sample. The C 1s peaks around 284.5 and 288.0 eV shown in Fig. 1d are ascribed to adventitious carbon used for calibration (sp^2 carbon) and the N-C-N bond of $\text{g-C}_3\text{N}_4$ (sp^3 carbon), respectively. Notably, there is a positive shift of sp^3 carbon peak from 288.0 eV of CN to 288.1 eV of H_2 -Ti-CN sample, which may be attributed to the hybridization effect of the heterostructure [9]. Fig. 1e reveals N 1s peaks around 398.7, 400.0, and 401.1 eV which are assigned to two-coordinated (N_{2c}) and three-coordinated (N_{3c}) nitrogen atoms, and NHx groups, respectively, which is in good agreement with previous results [48]. In the case of Ti-CN and H_2 -Ti-CN samples, it was observed that the peak-area ratio of $\text{N}_{2c}/\text{N}_{3c}$ decreased, indicating a preferential loss of N_{2c} atoms. The increase in the N-vacancy concentration of H_2 -Ti-CN, in line with the EPR conclusion, is caused by the unsaturated coordination resulting from the preferential loss of N_{2c} atoms [44]. When without UV light illumination, the binding energies of the O 1s and Ti 2p peaks in the heterojunction shift to lower energy levels, indicating an increase in electronic density in TiO_2 [49]. In contrast, the binding energy of the N 1s peak in the heterojunction shows a positive shift without UV light illumination, suggesting electron flow from CN to TiO_2 under dark condition. However, during in-situ XPS measurements under illumination, the binding energies of O 1s and Ti 2p peaks in the heterojunction significantly shift to higher energy levels (Fig. 1c, f), while binding energy of N 1s peak notably shifts to lower energy levels (Fig. 1e), indicating that photocarriers transfer from

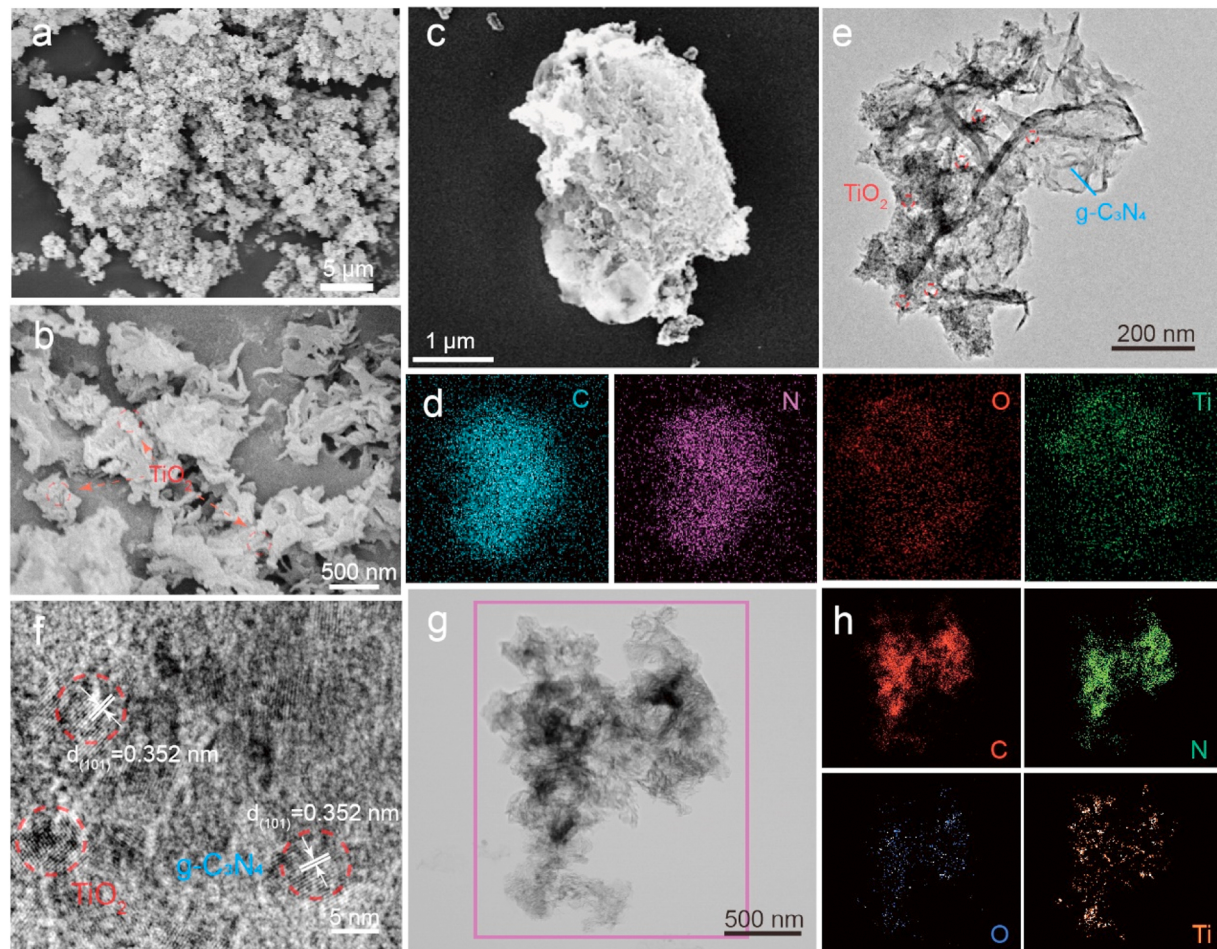


Fig. 2. (a) SEM images of Ti-CN. (b) SEM images of H_2 -Ti-CN (c-d) EDX element mapping of C, N, O and Ti elements for H_2 -Ti-CN (e-g) TEM images of H_2 -Ti-CN sample. (h) EDX mapping of C, N, O and Ti elements for H_2 -Ti-CN.

$\text{H}_2\text{-TiO}_2$ to $\text{H}_2\text{-CN}$ in the presence of light [50]. Therefore, the in-situ XPS results successfully reveal the charge transfer pathways at the heterojunction interface under illumination, aligning well with a S-scheme mechanism.

Fig. 2a and b show the SEM images of Ti-CN and $\text{H}_2\text{-Ti-CN}$, respectively. For SEM EDX elements mapping shown in Figs. 2c and 2d, the TiO_2 particles are dispersed on the surface of the porous CN nanosheets. After the H_2 reduction treatment, the structure of the $\text{H}_2\text{-Ti-CN}$ becomes more porous and looser. The TEM images of $\text{H}_2\text{-Ti-CN}$ are displayed in Figs. 2e, 2f, S3 and S4, where the size of TiO_2 particles is approximately 5–10 nm and they are uniformly dispersed on the surface of CN nanosheets. Fig. 2f demonstrates the close contact between TiO_2 and CN, providing evidence of the formation of heterojunctions and their mutual interaction. Figs. 2g and 2h shows the EDX elemental mappings of $\text{H}_2\text{-Ti-CN}$, revealing the homogeneous distribution of C, N, O, and Ti elements. These results further prove the existence of those elements in the TiO_2 nanoparticles that were deposited well onto the surface of CN during the hydrothermal synthesis and H_2 reduction process.

The photoelectric properties and PL emission spectroscopy were utilized to investigate the efficiency of the separation of photogenerated charges in the prepared samples. The photocurrent response test is an effective method to measure the efficiency of photocatalysts to generate photogenerated charges under light as well as the rate of charge separation. Fig. 3a shows the periodic photocurrent-time curve of $\text{H}_2\text{-CN}$, $\text{H}_2\text{-TiO}_2$ and $\text{H}_2\text{-Ti-CN}$ composites. It is evident that the photocurrent density of $\text{H}_2\text{-Ti-CN}$ composites is significantly higher than that of $\text{H}_2\text{-CN}$ and $\text{H}_2\text{-TiO}_2$, indicating a faster rate of charge separation and migration on the $\text{H}_2\text{-Ti-CN}$ composite. This conclusion is further supported by the electrochemical impedance spectroscopy (EIS) measurements (Fig. 3b), wherein a smaller radius corresponds to a higher interfacial charge transfer and separation efficiency [51]. It is clear that the Ti-CN and $\text{H}_2\text{-Ti-CN}$ exhibit a smaller EIS curve radius compared to the $\text{H}_2\text{-CN}$ and $\text{H}_2\text{-TiO}_2$ semiconductors, which proves that the construction of heterojunction is an effective method of reducing the recombination of photogenerated carriers. Moreover, after H_2 treatment, $\text{H}_2\text{-Ti-CN}$ exhibits the smallest radius, indicating an enhancement in the efficiency of e^-/h^+

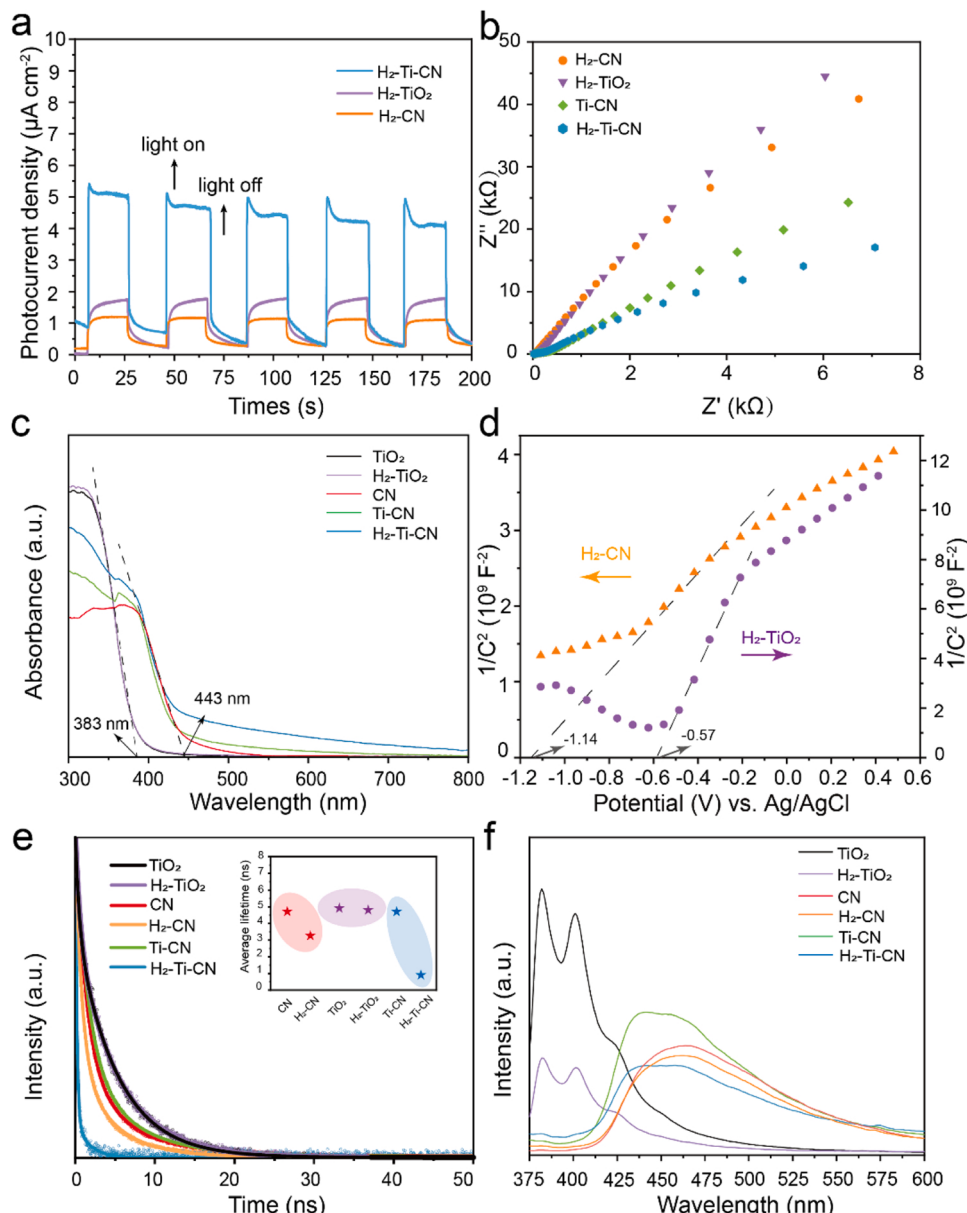


Fig. 3. Materials performance characterization. (a) Photocurrent response curves. (b) EIS spectra. (c) UV-Vis spectra. (d) Mott-Schottky curves. (e) TRPL spectra. (f) Steady-state PL spectra.

pairs separation through this process. The disparities in sunlight utilization and electronic band structure of the H₂-CN and H₂-TiO₂ were assessed using UV-Vis DRS and potential band analysis based on Mott-Schottky methods (as illustrated in Figs. 3c and 3d). The light absorption edges of TiO₂ and H₂-TiO₂ are both near 383 nm while the absorption edge of CN is around 443 nm. Of noteworthy mention is that upon the construction of the Ti-CN heterojunction, the absorption edge was extended to an area near that of CN. In addition, compared to CN, Ti-CN and H₂-Ti-CN demonstrated an enhancement in absorption intensity in the ultraviolet region, which confirms the existence of TiO₂ component, thus proving the strong binding between CN and TiO₂. Furthermore, in comparison to Ti-CN, the H₂-Ti-CN sample after hydrogen reduction treatment suggests stronger light absorption and utilization capabilities towards ultraviolet light as well as a portion of the visible region. The bandgap (E_g) can be calculated from the UV-Vis curve (see Fig. S5) and E_{CB} (E_{VB}=E_g+E_{CB}) [52]. The BET surface area of H₂-CN, H₂-TiO₂, and H₂-Ti-CN samples are shown in Fig. S6; it is clear that after constructing the Ti-CN heterojunction, the specific surface area increases to 106.8 m² g⁻¹, which could enhance the physical adsorption of CO₂, thereby enriching the photocatalyst surface with a higher density of CO₂ molecules and subsequently boosting the evolution rate of the product [53].

Photogenerated charge carrier transfer dynamics are investigated via TRPL decay spectra. As shown in Fig. 3e and Table S1, through a biexponential fitting of the TRPL spectra of the typical samples, the short lifetime (τ_1), the long lifetime (τ_2) and an average lifetime of the photogenerated carrier (τ_a) have been calculated, where the τ_1 corresponds to non-irradiative recombination while τ_2 corresponds to the free excitations recombination [54]. From the results, it can be observed that both CN and TiO₂ show a decreasing trend in τ_a after hydrogen reduction treatment. From CN to H₂-CN, the τ_a value decreased from 4.88 ns to 3.38 ns, while the change in τ_a for TiO₂ and H₂-TiO₂ was not significant, decreasing from 5.01 ns to 4.94 ns, suggesting a greater degree of unimpeded migration of photogenerated charges in CN or TiO₂ treated with H₂ reduction. Notably, the H₂-CN has a faster non-irradiative decay, compared with pristine CN, due to the introduction of nitrogen-vacancy [55]. As shown in Table S1, the H₂-Ti-CN sample shows a lower percentage of τ_2 (10%) than that of Ti-CN (29.4%), and moreover, the H₂-Ti-CN sample demonstrates a significant decrease in lifetime, from 4.81 ns to 0.92 ns, after undergoing H₂ reduction treatment. Simultaneously, the average lifetime of photogenerated charge carriers for H₂-Ti-CN is significantly shorter than that of H₂-CN and H₂-TiO₂ in Table S1. This is because in the S-scheme H₂-Ti-CN photocatalyst, ultrafast transfer at the interface from the CB of H₂-TiO₂ to the highest occupied molecule orbital (HOMO) of H₂-CN results in fewer electrons participating in radiative recombination. These findings validate that the dominant and effective reduction of excited charge recombination is attributed to charges being trapped in the mid-gap states as the defect count in the photocatalysts rises. This suggests the formation of rapid charge transfer channels within the defective heterojunction formed by these two semiconductors [56]. Consequently, treating the photocatalysts with the H₂ reduction process improves the charge separation efficiency, leading to a higher migration of electrons to the surface of the photocatalyst, thereby enhancing their participation in the reaction [57]. Meanwhile, the steady-state PL spectra shown in Fig. 3f presents the various signal intensity of prepared samples. It is evident that after TiO₂ undergoes hydrogen reduction treatment, more oxygen vacancies are exposed on the catalyst surface due to the sweeping of the hydrogen flow. This allows the photo-generated charge carriers to be transferred more quickly to the surface of the photocatalyst. As a result, the PL signal of the H₂-TiO₂ sample significantly decreases. Similarly, the H₂-CN also shows a decreases PL signal compared to CN. The PL curves of Ti-CN and H₂-Ti-CN clearly show that after TiO₂ is loaded onto CN, the peak position of PL shifts towards the middle of these two pristine semiconductors' peaks, providing evidence for the successful synthesis of Ti-CN hybrids. In addition, the lower

signal intensity means the H₂ reduction process of the H₂-Ti-CN sample is more conducive to suppressing the recombination of photogenerated carriers due to the construction of defects [58].

3.2. Photocatalytic performance

Photocatalytic activity and CH₄ selectivity of prepared samples are shown in Fig. 4a. The selectivity for CO and CH₄ was calculated according to the amount of electron transfer during the reaction. Relative calculations are as follows:

$$S_{CH_4}\% = [8*R(CH_4)]/[2*R(CO)+ 8*R(CH_4)] *100\% \quad (1)$$

$$S_{CO}\% = [2*R(CO)]/[2*R(CO)+ 8*R(CH_4)] *100\% \quad (2)$$

Where the R(CO) represents the yield of CO while the R(CH₄) represents the yield of CH₄. Fig. 4a clearly showed that CO was the main product of photocatalytic CO₂ reduction for CN and H₂-CN with relatively lower CH₄ selectivity below 45%. Compared to TiO₂, the CO and CH₄ yields of H₂-TiO₂ had approximately doubled, which can be attributed to the increased active sites of oxygen vacancies on the surface of H₂-TiO₂ due to H₂ sweeping. Furthermore, the ¹H NMR results in Fig. S7 supported this observation by demonstrating that H₂-TiO₂ had fewer surface hydroxyl groups after H₂ reduction, leading to the exposure of more active sites and an improvement in photocatalytic performance. Fig. S8 shows the activity of prepared samples with different mass ratios and the samples with or without H₂ treatment. Also, the photocatalytic performance of mixed H₂-TiO₂/H₂-CN samples is significantly lower than that of samples forming heterojunctions in Fig. S8. We further conducted control experiments regarding the vacancy content and performance in Fig. S9, and the results indicate that the sample with an appropriate content of vacancies has the best performance. The results show that the H₂-25Ti-CN presents the highest CH₄ evolution rate and selectivity; thus the sample named H₂-Ti-CN in Fig. 4a is the sample H₂-25Ti-CN in the Fig. S8. Notably, the CH₄ selectivity of the Ti-CN sample (61.5%) had improved compared to pristine CN (41.3%) attributed to the loading of a certain amount of higher methane-selective TiO₂. Additionally, the formation of a heterojunction reduced the recombination of photo-generated charge carriers, thereby enhancing photocatalytic performance. Interestingly, the H₂-Ti-CN sample showed a significant improvement in photocatalytic performance after the H₂ reduction treatment. The methane production increased from 3.5 to 27.4 μmol g⁻¹ h⁻¹, nearly an eight-fold increase, with CH₄ selectivity reaching 93.6%. Considering the previous characterization results, the remarkable performance enhancement was primarily attributed to the synergistic effect of nitrogen vacancies in CN and oxygen vacancies in TiO₂. Considering that CN itself contains carbon (C element), to determine the carbon source of the reaction product, gas chromatography-mass spectrometry (GC-MS) was employed for detection. 13CH₄ (m/z = 17) is the main product with 13CO₂ as the carbon source in Fig. S10, showing the reaction products of H₂-Ti-CN in the CO₂ reduction process come from CO₂. Additionally, the formation of a heterojunction between the two semiconductors facilitated the efficient transfer of electrons/holes to the surface of the photocatalysts, enhancing the overall photocatalytic activity [59]. The 24-hour stability test of H₂-Ti-CN for performance and selectivity was shown in Fig. 4b. The test consists of six cycles, with measurements taken every 4 h. It can be observed that after the six cycles, methane production decreases by just about 10%, while the selectivity remains around 93.2%. Based on these results, it can be concluded that H₂-Ti-CN exhibits excellent stability under long-time solar illumination. To further verify the heterostructure of the H₂-Ti-CN sample, the ESR analysis was performed by using 5,5-dimethyl-1-pyrroline N-oxide (DMPO) as a spin-trapping agent for superoxide and hydroxyl radicals (•O₂ and •OH) under low temperature and UV-vis light for 10 min. The characteristic peaks in Fig. 4c, after the analysis of DMPO-•O₂, demonstrate the H₂-CN sample (E_{CB} = -1.14 eV) had a stronger signal intensity than the H₂-TiO₂ sample (E_{CB} = -0.57

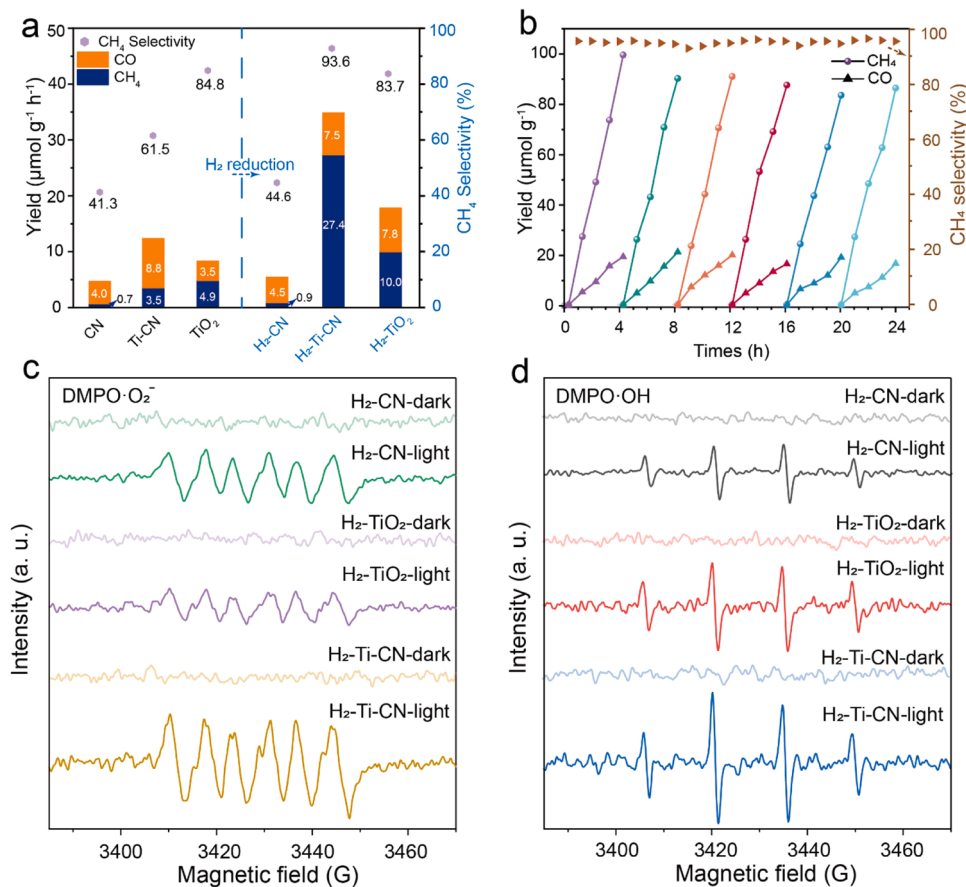


Fig. 4. Performance of photocatalytic CO_2 reduction. (a) The activity of CO_2 photoreduction, (b) stability testing for 24 h (6 cycles). ESR signals of $\text{H}_2\text{-TiO}_2$, $\text{H}_2\text{-CN}$, $\text{H}_2\text{-Ti-CN}$ (c) in methanol dispersion for DMPO-superoxide radical and (d) in aqueous dispersion for DMPO-hydroxyl radical under low temperature and UV-vis light for 10 min, respectively.

eV). These findings indicate that $\text{H}_2\text{-CN}$ tends to be the reduction side of heterostructure compared to $\text{H}_2\text{-TiO}_2$. In the analysis of DMPO- $\cdot\text{OH}$ (Fig. 4 d), $\text{H}_2\text{-CN}$ ($\text{VB} = 1.52$ eV) exhibited weak signal intensity, while $\text{H}_2\text{-TiO}_2$ ($\text{VB} = 2.52$ eV) showed stronger signal intensity, indicating that the oxidation side tends to occur in $\text{H}_2\text{-TiO}_2$, which aligns with their measured different oxidation potentials[60]. In addition, after loading $\text{H}_2\text{-TiO}_2$, the heterojunction sample could still produce $\cdot\text{O}_2^-$ and $\cdot\text{OH}$, proving that the photoinduced e^- on the CB of $\text{H}_2\text{-CN}$ and h^+ on the VB of $\text{H}_2\text{-TiO}_2$ were able to stay there to drive the redox reactions. The ESR results indicate the successful formation of a heterojunction, which facilitates the generation of superoxide and hydroxyl radicals, further confirming the construction of S-scheme heterojunction for the $\text{H}_2\text{-Ti-CN}$ sample.

3.3. Gibbs free energy calculation

Optimizing the desorption/adsorption process and hydrogenation of intermediates allows for the adjustment of the Gibbs free energy of intermediates, thereby achieving regulation of activity and selectivity [61, 62]. The reduction of CO_2 to CH_4 involves the transfer of eight proton-electron pairs ($\text{H}^+ + \text{e}^-$), and the adsorption of various intermediate species on the surface can significantly impact the efficiency and selectivity of CO_2 reduction [63]. To facilitate the understanding of the highly selective reduction of CO_2 to CH_4 by $\text{H}_2\text{-Ti-CN}$ heterojunction, intermediates involved in the CO_2 activation/conversion process on the photocatalyst surface were investigated using the in-situ DRIFTS to guide DFT theoretical modeling. As shown in Fig. 5a, no peaks were observed under dark conditions. Upon introducing light illumination into the testing system, significant changes in the DRIFTS signals were

observed. Specifically, with time increasing, a characteristic peak attributed to the $\cdot\text{CO}_2$ species appeared at 1645 cm^{-1} . Two signals detected at 1299 cm^{-1} and 1464 cm^{-1} involving $\cdot\text{COOH}$ and ${}^*\text{HCO}_3$ reflected the conversion of ${}^*\text{CO}_2$ to ${}^*\text{COOH}$ [64]. The signal at 2080 cm^{-1} represented the intermediate ${}^*\text{CO}$ species. Furthermore, the peaks at 1165 cm^{-1} and 1360 cm^{-1} indicated the further hydrogenation of ${}^*\text{CO}$, which is a crucial intermediate for CH_4 production [61]. The intensity of the intermediate peaks eventually reached a stable state with increasing time, suggesting a dynamic equilibrium between the adsorption/activation and conversion of CO_2 on the photocatalyst under light irradiation [64]. Based on the supporting DRIFTS results mentioned above, we further investigated the mechanism of the heterojunction's high selectivity through DFT calculations.

Generally, the initial hydrogenation of CO_2 to form the ${}^*\text{COOH}$ radical requires a substantial amount of energy in an isolated conversion process [65]. For instance, the $\text{TiO}_2/\text{g-C}_3\text{N}_4$ heterojunction discovered a change in the reaction barrier from 0.65 eV to 0.37 eV before and after the introduction of H_2 reduction treatment as shown in Figs. 5b and 5c. Subsequently, the ${}^*\text{COOH}$ radical undergoes hydrogenation and loses H_2O to form the ${}^*\text{CO}$ intermediate. The adsorption model clearly demonstrates that vacancies can serve as ideal active sites for effectively capturing the C atoms of ${}^*\text{COOH}$, ${}^*\text{CO}$, and capturing O atoms of ${}^*\text{CH}_3\text{O}$ intermediates on the surface. Therefore, vacancies, as active sites, enhance adsorption, facilitating further hydrogenation reactions of the intermediates. Conversely, non-vacancy sites tend to lead to easier desorption of intermediate products from the surface. Notably, the optimized slab model indicates weak ${}^*\text{CO}$ adsorption, which makes ${}^*\text{CO}$ more susceptible to desorption, resulting in the formation of product CO . Consequently, the vacancies generated by H_2 reduction-mediated

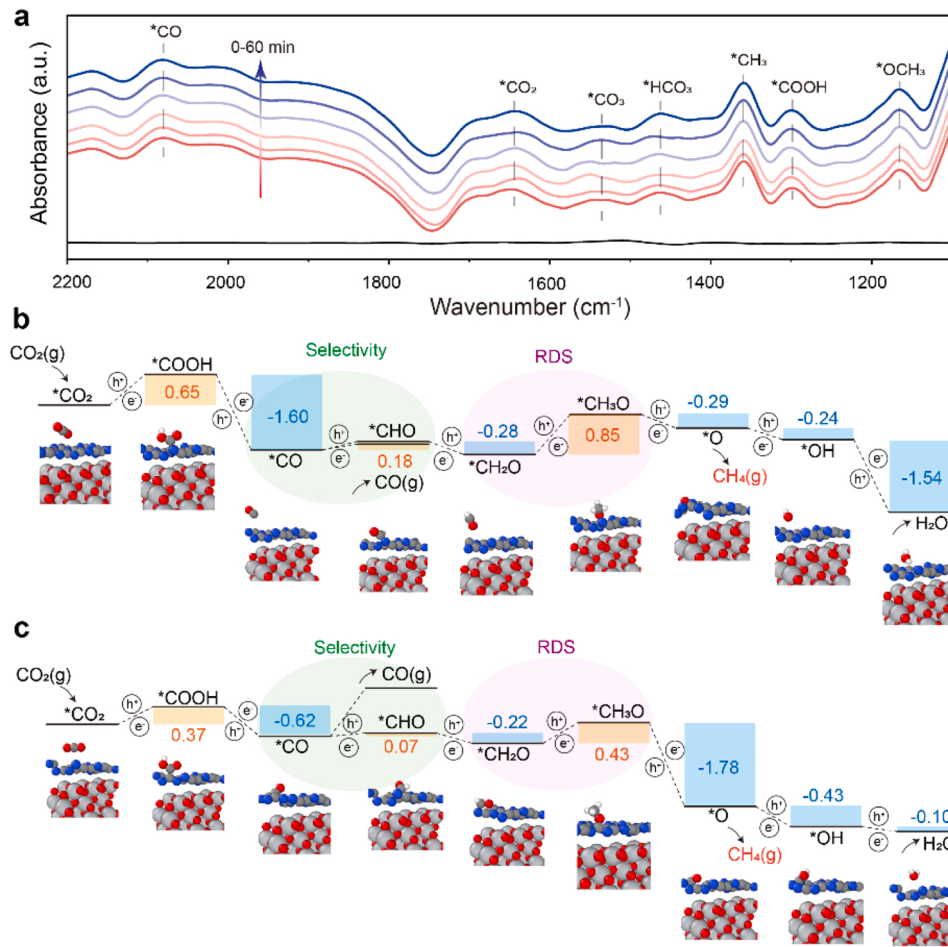


Fig. 5. (a) In situ FT-IR and free energy diagram of CO₂ reduction to CO and CH₄ on H₂-Ti-CN heterojunction (b) without and (c) with vacancy. The green region represents the area where selectivity is enhanced, specifically referring to the increased energy barrier for CO desorption when considering H₂ reduction. The purple region corresponds to the rate-determining step (RDS) for CO₂ reduction to CH₄, which is the conversion from *CH₂O to *CH₃O. The adsorption slab models of the corresponding intermediate species are shown below the reaction pathway. Different-colored spheres represent atoms of different elements, where red, light gray, dark gray, blue, and white represents O, Ti, C, N, and H, respectively.

heterojunctions effectively enhance intermediate adsorption, reducing the production of the two-electron product CO, and improving the selectivity of the eight-electron reaction (green region). Additionally, the reaction barriers for *CHO and *CH₃O intermediates are observed to be 0.18 eV and 0.85 eV, respectively. After the introduction of hydrogen reduction, the heterojunction exhibits a smooth reaction pathway for the remaining CO₂ reduction mechanisms. Notably, the conversion of *CH₂O→*CH₃O in both cases is associated with the highest energy barrier, indicating that the reaction step with fifth H⁺+e⁻ serves as the rate-determining step (RDS) (purple region). It is evident that the energy barrier of the RDS significantly decreases after the implementation of H₂ reduction, allowing CH₄ to be spontaneously released following the hydrogenation of *CH₃O, without any energy barrier. The generated gas CH₄, with *O still adsorbed on the surface, can facilitate the rapid spontaneous reactions necessary for the regeneration of the bare surface. Notably, both before and after H₂ reduction treatment on the heterojunction, *O can spontaneously convert to *OH and subsequently form and release H₂O, indicating that the reduction end can be refreshed on the surface after the completion of the eight-electron reaction. In conclusion, compared to other g-C₃N₄ based heterostructures preferring to reduce CO₂ to CO [66], this study with defective heterostructure modified by H₂ reduction is further studied by theoretical results, demonstrating high selectivity and activity in reducing CO₂ to CH₄.

3.4. Mechanism analysis

To gain a further understanding of H₂-Ti-CN heterojunctions, UPS was employed to investigate the VB and Fermi level (EF) of this photocatalyst. This aided in determining the heterojunction type of the photocatalyst and studying electron transport between the heterojunctions. As shown in Fig. 6a, the work function can be calculated by subtracting the secondary electron cutoff energy from the incident photon energy [67]. The work functions for the H₂-CN, H₂-TiO₂, and H₂-Ti-CN heterojunctions were determined to be 4.70 eV, 4.19 eV and 4.52 eV, respectively. Fig. 6b analyzed the VB region to obtain the relative positions of the VB. Combining the bandgap obtained from UV-Vis spectroscopy, the schematic illustration of the band structures was determined in Fig. 6c. When the heterojunction is formed, the Fermi level of H₂-CN is higher than that of H₂-TiO₂, causing free electrons to migrate from the H₂-CN side to the H₂-TiO₂ side until the Fermi levels match. As electrons move from H₂-CN to H₂-TiO₂, the energy bands bend, creating a built-in potential at the interface, as shown in Fig. 6c, with the internal electric field from H₂-CN to H₂-TiO₂. Under light illumination, both H₂-CN and H₂-TiO₂ generate electron-hole pairs. To gain a further understanding of the charge transfer dynamics within the H₂-Ti-CN S-scheme heterojunction after photoexcitation, fs-TAS measurements were conducted for H₂-CN and H₂-Ti-CN. For the two samples in Fig. 6d-e, a broad, negative profile (ranging from 440 to 570 nm) corresponding to the ground state bleach (GSB) of H₂-CN was observed

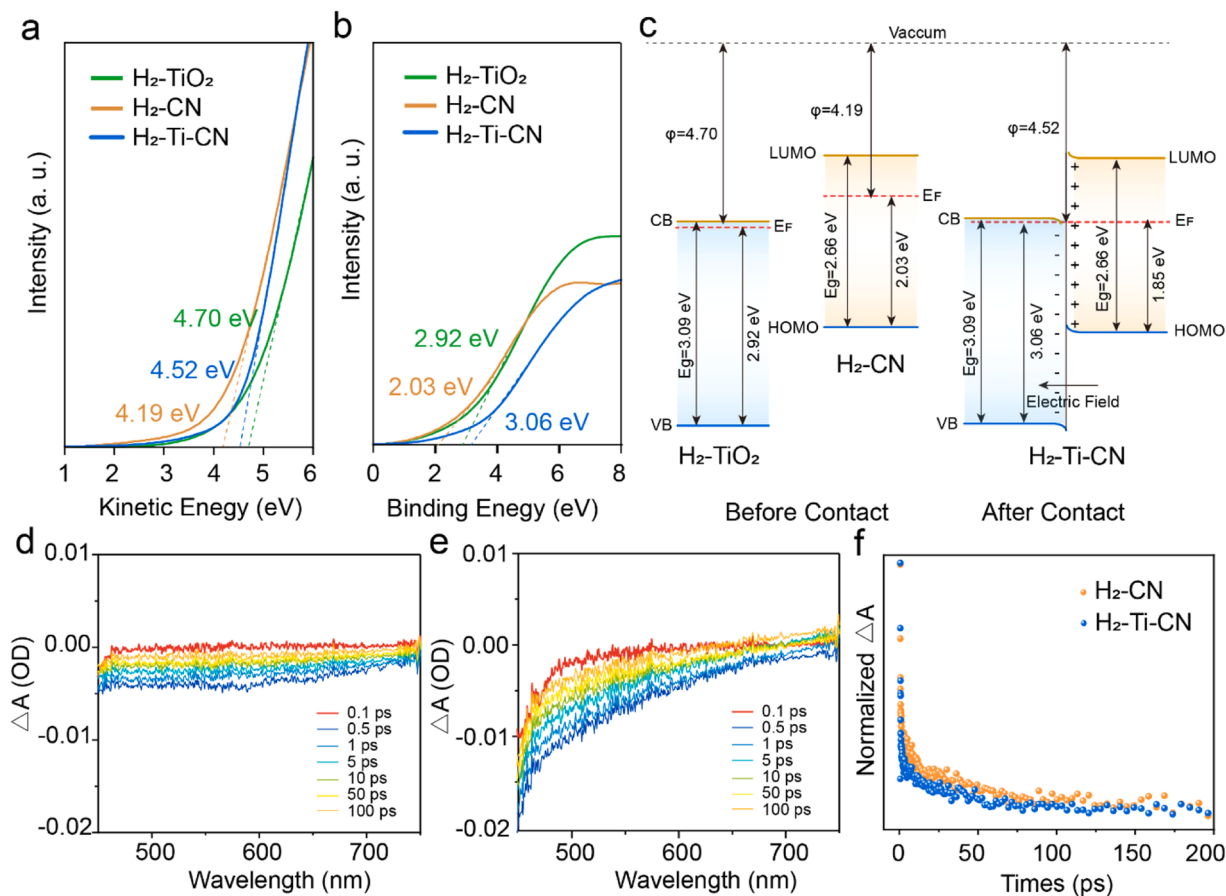


Fig. 6. UPS measurements for (a) work function from secondary electron cut-off and (b) valence band. (c) The schematic illustration of the band structures shows the proposed S-scheme heterojunction photocatalytic mechanism. The fs-TAS spectra of (d) H₂-CN and (e) H₂-Ti-CN measured with 400 nm excitation and corresponding transient absorption kinetic. (f) The fs-TAS kinetics lifetimes from 0 to 200 ps.

[68]. H₂-Ti-CN exhibited a stronger fs-TAS signal, indicating an increased number of photo-generated electrons in the heterojunction system [69]. To investigate the interface charge transfer within H₂-Ti-CN, the fs-TAS kinetics lifetimes were plotted in Fig. 6f and fitted by using a double-exponential equation. The fitting parameters are provided in Table S2, where the decay component τ_1 reveals the trapping of electrons from the CB into the trapped state, while component τ_2 represents the recombination of trapped electrons and holes [70]. The slower decay observed in H₂-Ti-CN samples suggests a longer carrier lifetime in the heterojunction. Compared to H₂-CN, the lifetime of H₂-Ti-CN is significantly shortened, which can be attributed to efficient electron transfer induced by the superexchange effect [71]. Furthermore, the accelerated time constant τ_1 of H₂-Ti-CN also demonstrates rapid charge capture in S-scheme heterojunction. TRPL conclusions are consistent with fs-TAS analysis, indicating that this S-scheme heterojunction with vacancies both promote charge capture and carrier transfer processes. Subsequently, the charge density difference ($\Delta\rho$) was calculated for heterojunctions with no vacancies, where $\Delta\rho = \rho(\text{TiO}_2/\text{CN}) - \rho(\text{TiO}_2) - \rho(\text{CN})$, and compared with H₂-Ti-CN with dual vacancies. This further elucidated the crucial role of dual vacancies in promoting charge transfer (Fig. S11). The $\Delta\rho$ visualized through contour plots showed a more significant charge redistribution at the H₂-Ti-CN interface, particularly in the vicinity of vacancies, which opens the ultrafast interfacial charge transfer channel and facilitates electron migration between charge transfer pathways [72]. Through the S-scheme process, charge carriers are effectively separated in energy bands with a strong redox potential. The band structure analysis, in combination with previous characterization and DFT calculation, confirmed the S-scheme of the heterojunction with ultrafast interfacial

charge transfer.

4. Conclusions

In this study, we successfully constructed defect-induced ultrafast charge transfer channels in TiO₂/g-C₃N₄ heterojunction through low-temperature H₂ reduction treatment. Based on defect analysis using XPS, EPR and ESR, the vacancy concentration in the Ti-CN sample significantly increased after the H₂ sweeping reduction treatment. Characterization methods such as PL, TRPL, fs-TAS and EIS revealed that these defects fostered ultrafast charge carrier transfer channels, amplified the interaction at heterojunction interfaces. Additionally, H₂ reduction of the photocatalyst is believed to facilitate the transfer of light-excited charges to the surface, thereby enhancing its high redox capabilities in catalytic reactions. Benefiting from the advantages, defect-rich H₂-Ti-CN exhibited a CO₂-to-CH₄ selectivity of 93.6% and a CH₄ yield of 27.4 μmol g⁻¹ h⁻¹, which were approximately 39.1, 5.59, and 7.8 times higher than that of pre-H₂-treated CN, TiO₂, and Ti-CN, respectively. Furthermore, H₂-Ti-CN demonstrated excellent stability and maintained high methane selectivity during 24 h of solar irradiation. In situ DRIFT and DFT results also indicated a thermodynamic preference for CH₄ release on the H₂-Ti-CN heterojunction, considering the synergistic effect of heterojunction and defects. This work provides a new perspective on photocatalyst modification strategies by using a low-temperature (300 °C) H₂ sweeping reduction approach to remove surface hydroxyl accumulation and introduce vacancies to promote charge separation and transfer to the surface and enhance performance (photocatalytic activity and selectivity). The H₂ reduction-assisted defect-enhanced strategy for constructing S-scheme heterojunction paves the

way for material innovation in developing photocatalytic selective CO₂ reduction.

CRediT authorship contribution statement

Shuwen Cheng: Conceptualization, Investigation, Writing – original draft. **Zhehao Sun, Zongyou Yin:** Software, Investigation, Resources, Writing – review & editing. **Kang Hui Lim:** Investigation, Review & editing. **Tao Du, Liying Liu:** Review & editing. **Ary Anggara Wibowo, Kaili Liu, Hieu T. Nguyen:** Formal analysis. **Gang Li:** Funding acquisition, Supervision, Review & editing. **Kawi Sibudjing:** Funding acquisition, Project administration, Review & editing, Supervision.

Declaration of Competing Interest

The authors declare that they have no known competing financial interests or personal relationships that could have appeared to influence the work reported in this paper.

Data availability

Data will be made available on request.

Acknowledgement

The authors acknowledge the financial support from A*STAR LCERFI Project (Award ID: U2102d2011; WBS: A-8000278-00-00), the Singapore Ministry of Education Academic Research Fund Tier 1 Project (WBS: A-0009184-00-00), the National Natural Science Foundation of China (grant number 22078054), the China Scholarship Council (CSC) program, and the Australian Research Council Discovery Project (DP200100159). The DFT calculations are undertaken with the support of resources provided by the National Computational Infrastructure (NCI) facilities at the Australian National University, which are allocated through the 2023 National Computational Merit Allocation Scheme (NCMAS) and Adapter Allocation Scheme.

Appendix A. Supporting information

The authors have cited additional references within the Supporting Information. Supplementary data associated with this article can be found in the online version at [doi:10.1016/j.apcatb.2023.123583](https://doi.org/10.1016/j.apcatb.2023.123583).

References

- [1] H. Rao, L.C. Schmidt, J. Bonin, M. Robert, Visible-light-driven methane formation from CO₂ with a molecular iron catalyst, *Nature* 548 (2017) 74–77.
- [2] S. Das, J. Pérez-Ramírez, J. Gong, N. Dewangan, K. Hidajat, B.C. Gates, S. Kawi, Core-shell structured catalysts for thermocatalytic, photocatalytic, and electrocatalytic conversion of CO₂, *Chem. Soc. Rev.* 49 (2020) 2937–3004.
- [3] T. Zhang, F. Meng, M. Gao, J. Wei, K.J.H. Lim, K.H. Lim, P. Chirawatkul, A.S. W. Wong, S. Kawi, G.W. Ho, Porous host–guest mof-semiconductor hybrid with multisites heterojunctions and modulable electronic band for selective photocatalytic CO₂ conversion and H₂ evolution, *Small* 19 (2023) 2301121.
- [4] Z. Jiang, X. Xu, Y. Ma, H.S. Cho, D. Ding, C. Wang, J. Wu, P. Olynykiv, M. Jia, J. Cheng, Y. Zhou, O. Terasaki, T. Peng, L. Zan, H. Deng, Filling metal-organic framework mesopores with TiO₂ for CO₂ photoreduction, *Nature* 586 (2020) 549–554.
- [5] H. Chen, C.E. Nanayakkara, V.H. Grassian, Titanium dioxide photocatalysis in atmospheric chemistry, *Chem. Rev.* 112 (2012) 5919–5948.
- [6] Z.-W. Wang, Q. Wan, Y.-Z. Shi, H. Wang, Y.-Y. Kang, S.-Y. Zhu, S. Lin, L. Wu, Selective photocatalytic reduction CO₂ to CH₄ on ultrathin TiO₂ nanosheet via coordination activation, *Appl. Catal. B Environ.* 288 (2021), 120000.
- [7] P. Chen, Xa Dong, M. Huang, K. Li, L. Xiao, J. Sheng, S. Chen, Y. Zhou, F. Dong, Rapid self-decomposition of g-C₃N₄ during gas-solid photocatalytic CO₂ reduction and its effects on performance assessment, *ACS Catal.* 12 (2022) 4560–4570.
- [8] M. Ou, W. Tu, S. Yin, W. Xing, S. Wu, H. Wang, S. Wan, Q. Zhong, R. Xu, Amino-assisted anchoring of CsPbBr₃ perovskite quantum dots on porous g-C₃N₄ for enhanced photocatalytic CO₂ reduction, *Angew. Chem. Int. Ed. Engl.* 57 (2018) 13570–13574.
- [9] H. Guo, T. Zhang, W. Ma, S. Cheng, J. Ding, Q. Zhong, S. Kawi, Construction of sandwich-like Ag/UiO-66@g-C₃N₄ Z-scheme ternary heterojunction for photocatalytic CO₂ conversion to CH₃OH and CO, *Fuel* 344 (2023), 127911.
- [10] T. Zhang, T. Wang, F. Meng, M. Yang, S. Kawi, Recent advances in ZnIn₂S₄-based materials towards photocatalytic purification, solar fuel production and organic transformations, *J. Mater. Chem. C* 10 (2022) 5400–5424.
- [11] P. Hongmanorom, J. Ashok, G. Zhang, Z. Bian, M.H. Wai, Y. Zeng, S. Xi, A. Borgna, S. Kawi, Enhanced performance and selectivity of CO₂ methanation over phyllosilicate structure derived Ni-Mg/SBA-15 catalysts, *Appl. Catal. B Environ.* 282 (2021), 119564.
- [12] F. Hu, R. Ye, C. Jin, D. Liu, X. Chen, C. Li, K.H. Lim, G. Song, T. Wang, G. Feng, R. Zhang, S. Kawi, Ni nanoparticles enclosed in highly mesoporous nanofibers with oxygen vacancies for efficient CO₂ methanation, *Appl. Catal. B Environ.* 317 (2022), 121715.
- [13] S. Das, K.H. Lim, T.Z.H. Gani, S. Aksari, S. Kawi, Bi-functional CeO₂ coated NiCo-MgAl core-shell catalyst with high activity and resistance to coke and H₂S poisoning in methane dry reforming, *Appl. Catal. B Environ.* 323 (2023), 122141.
- [14] Y. Zhu, Selective CH₄ production from CO₂ photoreduction via single-atom-promoted H₂O dissociation, *Chem. Catal.* 3 (2023), 100783.
- [15] Y. Wang, H. Huang, Z. Zhang, C. Wang, Y. Yang, Q. Li, D. Xu, Lead-free perovskite Cs₂AgBiBr₆@g-C₃N₄ Z-scheme system for improving CH₄ production in photocatalytic CO₂ reduction, *Appl. Catal. B Environ.* 282 (2021), 119570.
- [16] T. Zhang, F. Meng, M. Gao, W.L. Ong, K.-G. Haw, T. Ding, G.W. Ho, S. Kawi, Multi-interfacial catalyst with spatially defined redox reactions for enhanced pure water photothermal hydrogen production, *EcoMat 3* (2021), e12152.
- [17] Y. Liu, F. Yu, F. Wang, S. Bai, G. He, Construction of Z-scheme In₂S₃-TiO₂ for CO₂ reduction under concentrated natural sunlight, *Chin. J. Struct. Chem.* 41 (2022) 2201034–2201039.
- [18] B. Zhao, Y. Zhao, P. Liu, Y. Men, X. Meng, Y. Pan, Progress and understanding on catalysts with well-defined interface for boosting CO₂ conversion, *Chin. J. Struct. Chem.* 41 (2022) 2204012–2204021.
- [19] Q. Li, Y. Ouyang, H. Li, L. Wang, J. Zeng, Photocatalytic conversion of methane: recent advancements and prospects, *Angew. Chem. Int. Ed.* 61 (2022), e202108069.
- [20] P. Hongmanorom, J. Ashok, P. Chirawatkul, S. Kawi, Interfacial synergistic catalysis over Ni nanoparticles encapsulated in mesoporous ceria for CO₂ methanation, *Appl. Catal. B Environ.* 297 (2021), 120454.
- [21] H. Li, Y. Gao, X. Wu, P.-H. Lee, K. Shih, Fabrication of heterostructured g-C₃N₄/Ag-TiO₂ hybrid photocatalyst with enhanced performance in photocatalytic conversion of CO₂ under simulated sunlight irradiation, *Appl. Surf. Sci.* 402 (2017) 198–207.
- [22] Y. Wang, L. Rao, P. Wang, Z. Shi, L. Zhang, Photocatalytic activity of N-TiO₂/O-doped N vacancy g-C₃N₄ and the intermediates toxicity evaluation under tetracycline hydrochloride and Cr(VI) coexistence environment, *Appl. Catal. B Environ.* 262 (2020), 118308.
- [23] J. Low, Y. Ju, M. Jaroniec, S. Wageh, A.A. Al-Ghamdi, Heterojunction photocatalysts, *Adv. Mater.* 29 (2017) 1601694.
- [24] H. Wang, L. Zhang, Z. Chen, J. Hu, S. Li, Z. Wang, J. Liu, X. Wang, Semiconductor heterojunction photocatalysts: design, construction, and photocatalytic performances, *Chem. Soc. Rev.* 43 (2014) 5234–5244.
- [25] H. Lin, Y. Liu, Z. Wang, L. Ling, H. Huang, Q. Li, L. Cheng, Y. Li, J. Zhou, K. Wu, J. Zhang, T. Zhou, Enhanced CO₂ photoreduction through spontaneous charge separation in end-capping assembly of heterostructured covalent-organic frameworks, *Angew. Chem. Int. Ed.* 61 (2022), e202214142.
- [26] R. Acharya, K. Parida, A review on TiO₂/g-C₃N₄ visible-light-responsive photocatalysts for sustainable energy generation and environmental remediation, *J. Environ. Chem. Eng.* 8 (2020), 103896.
- [27] H. Shi, J. Du, J. Hou, W. Ni, C. Song, K. Li, G.G. Gurzadyan, X. Guo, Solar-driven CO₂ conversion over Co²⁺ doped 0D/2D TiO₂/g-C₃N₄ heterostructure: Insights into the role of Co²⁺ and cocatalyst, *J. CO₂ Util.* 38 (2020) 16–23.
- [28] C. Liu, F. Raziq, Z. Li, Y. Qu, A. Zada, L. Jing, Synthesis of TiO₂/g-C₃N₄ nanocomposites with phosphate–oxygen functional bridges for improved photocatalytic activity, *Chin. J. Catal.* 38 (2017) 1072–1078.
- [29] P. Ning, H. Chen, J. Pan, J. Liang, L. Qin, D. Chen, Y. Huang, Surface defect-rich g-C₃N₄/TiO₂ Z-scheme heterojunction for efficient photocatalytic antibiotic removal: rational regulation of free radicals and photocatalytic mechanism, *Catal. Sci. Technol.* 10 (2020) 8295–8304.
- [30] W. Gan, J. Guo, X. Fu, M. Zhang, C. Ding, Y. Hai, Y. Lu, J. Li, Z. Li, Z. Sun, Dual-defects modified ultrathin 2D/2D TiO₂/g-C₃N₄ heterojunction for efficient removal of levofloxacin: Performance, degradation pathway, and mechanism, *Sep. Purif. Technol.* 306 (2023), 122578.
- [31] H. Wang, H. Li, Z. Chen, J. Li, X. Li, P. Huo, Q. Wang, TiO₂ modified g-C₃N₄ with enhanced photocatalytic CO₂ reduction performance, *Solid State Sci.* 100 (2020), 106099.
- [32] X. Bao, D. Lu, Z. Wang, H. Yin, B. Zhu, B. Chen, M. Shi, Y. Zhang, Q. Xu, Y. Qin, Significantly enhanced photothermal catalytic CO₂ reduction over TiO₂/g-C₃N₄ composite with full spectrum solar light, *J. Colloid Interface Sci.* 638 (2023) 63–75.
- [33] B. Yu, F. Meng, M.W. Khan, R. Qin, X. Liu, Facile synthesis of AgNPs modified TiO₂@g-C₃N₄ heterojunction composites with enhanced photocatalytic activity under simulated sunlight, *Mater. Res. Bull.* 121 (2020), 110641.
- [34] H. Bian, D. Li, S. Wang, J. Yan, S.F. Liu, 2D-C₃N₄ encapsulated perovskite nanocrystals for efficient photo-assisted thermocatalytic CO₂ reduction, *Chem. Sci.* 13 (2022) 1335–1341.
- [35] H. Bian, T. Liu, D. Li, Z. Xu, J. Lian, M. Chen, J. Yan, S. Frank Liu, Unveiling the effect of interstitial dopants on CO₂ activation over CsPbBr₃ catalyst for efficient photothermal CO₂ reduction, *Chem. Eng. J.* 435 (2022), 135071.

- [36] X. Chen, R. Shi, Q. Chen, Z. Zhang, W. Jiang, Y. Zhu, T. Zhang, Three-dimensional porous g-C₃N₄ for highly efficient photocatalytic overall water splitting, *Nano Energy* 59 (2019) 644–650.
- [37] G. Kresse, J. Furthmüller, Efficiency of ab-initio total energy calculations for metals and semiconductors using a plane-wave basis set, *Comput. Mater. Sci.* 6 (1996) 15–50.
- [38] G. Kresse, J. Furthmüller, Efficient iterative schemes for ab initio total-energy calculations using a plane-wave basis set, *Phys. Rev. B* 54 (1996) 11169.
- [39] P.E. Blöchl, Projector augmented-wave method, *Phys. Rev. B* 50 (1994) 17953.
- [40] J.P. Perdew, K. Burke, M. Ernzerhof, Generalized gradient approximation made simple, *Phys. Rev. Lett.* 77 (1996) 3865.
- [41] S. Grimme, J. Antony, S. Ehrlich, H. Krieg, A consistent and accurate ab initio parametrization of density functional dispersion correction (DFT-D) for the 94 elements H-Pu, *The, J. Chem. Phys.* 132 (2010), 154104.
- [42] S. Cheng, Z. Sun, K.H. Lim, T. Zhang, E. Hondo, T. Du, L. Liu, M. Judd, N. Cox, Z. Yin, G.K. Li, S. Kawi, BiOCl nanoflowers with high levels of oxygen vacancy for photocatalytic CO₂ reduction, *ACS Appl. Nano Mater.* 6 (2023) 3608–3617.
- [43] X. Bi, G. Du, A. Kalam, D. Sun, Y. Yu, Q. Su, B. Xu, A.G. Al-Sehemi, Tuning oxygen vacancy content in TiO₂ nanoparticles to enhance the photocatalytic performance, *Chem. Eng. Sci.* 234 (2021), 116440.
- [44] Z. Wang, Y. Huang, M. Chen, X. Shi, Y. Zhang, J. Cao, W. Ho, S.C. Lee, Roles of N-vacancies over porous g-C₃N₄ microtubes during photocatalytic NO_x Removal, *ACS Appl. Mater. Interfaces* 11 (2019) 10651–10662.
- [45] L. Yan, J. Qin, B. Liang, Q. Wang, M. Geng, High-pressure induction and quantitative regulation of oxygen vacancy defects in lithium titanate, *Adv. Funct. Mater.* 33 (2023), 2301886.
- [46] J. Ding, W. Xu, H. Wan, D. Yuan, C. Chen, L. Wang, G. Guan, W.-L. Dai, Nitrogen vacancy engineered graphitic C₃N₄-based polymers for photocatalytic oxidation of aromatic alcohols to aldehydes, *Appl. Catal. B Environ.* 221 (2018) 626–634.
- [47] S. Cheng, Z. Sun, K.H. Lim, A.A. Wibowo, T. Zhang, T. Du, L. Liu, H.T. Nguyen, G. K. Li, Z. Yin, S. Kawi, Dual-defective two-dimensional/two-dimensional Z-scheme heterojunctions for CO₂ reduction, *ACS Catal.* (2023) 7221–7229.
- [48] W. Tu, Y. Xu, J. Wang, B. Zhang, T. Zhou, S. Yin, S. Wu, C. Li, Y. Huang, Y. Zhou, Z. Zou, J. Robertson, M. Kraft, R. Xu, Investigating the role of tunable nitrogen vacancies in graphitic carbon nitride nanosheets for efficient visible-light-driven H₂ evolution and CO₂ reduction, *ACS Sustain. Chem. Eng.* 5 (2017) 7260–7268.
- [49] F. Xu, K. Meng, B. Cheng, S. Wang, J. Xu, J. Yu, Unique S-scheme heterojunctions in self-assembled TiO₂/CsPbBr₃ hybrids for CO₂ photoreduction, *Nat. Commun.* 11 (2020) 4613.
- [50] L. Wang, B. Cheng, L. Zhang, J. Yu, In situ irradiated XPS investigation on S-scheme TiO₂@ZnIn₂S₄ photocatalyst for efficient photocatalytic CO₂ reduction, *Small* 17 (2021), 2103447.
- [51] H. Guo, S. Wan, Y. Wang, W. Ma, Q. Zhong, J. Ding, Enhanced photocatalytic CO₂ reduction over direct Z-scheme NiTiO₃/g-C₃N₄ nanocomposite promoted by efficient interfacial charge transfer, *Chem. Eng. J.* 412 (2021), 128646.
- [52] J. Jiang, X. Wang, Q. Xu, Z. Mei, L. Duan, H. Guo, Understanding dual-vacancy heterojunction for boosting photocatalytic CO₂ reduction with highly selective conversion to CH₄, *Appl. Catal. B Environ.* 316 (2022), 121679.
- [53] R. Nematollahi, C. Ghobbi, F. Khorasheh, A. Larimi, Ni-Bi co-doped TiO₂ as highly visible light response nano-photocatalyst for CO₂ photo-reduction in a batch photo-reactor, *J. CO₂ Util.* 41 (2020), 101289.
- [54] M. Tan, Y. Ma, C. Yu, Q. Luan, J. Li, C. Liu, W. Dong, Y. Su, L. Qiao, L. Gao, Q. Lu, Y. Bai, Boosting photocatalytic hydrogen production via interfacial engineering on 2D ultrathin Z-scheme ZnIn₂S₄/g-C₃N₄ heterojunction, *Adv. Funct. Mater.* 32 (2021), 2111740.
- [55] P. Yang, L. Wang, H. Zhuzhang, R. Wang, M.-M. Titirici, X. Wang, Photocarving nitrogen vacancies in a polymeric carbon nitride for metal-free oxygen synthesis, *Appl. Catal. B Environ.* 256 (2019), 117794.
- [56] Q. Zhou, Y. Guo, Z. Ye, Y. Fu, Y. Guo, Y. Zhu, Carbon nitride photocatalyst with internal electric field induced photogenerated carriers spatial enrichment for enhanced photocatalytic water splitting, *Mater. Today* 58 (2022) 100–109.
- [57] C. Cheng, B. He, J. Fan, B. Cheng, S. Cao, J. Yu, An inorganic/organic S-scheme heterojunction H₂ production photocatalyst and its charge transfer mechanism, *Adv. Mater.* 33 (2021), e2100317.
- [58] T. Zhang, F. Meng, Y. Cheng, N. Dewangan, G.W. Ho, S. Kawi, Z-scheme transition metal bridge of Co₃S₈/Cd/CdS tubular heterostructure for enhanced photocatalytic hydrogen evolution, *Appl. Catal. B Environ.* 286 (2021), 119853.
- [59] A.Y. Nosaka, E. Kojima, T. Fujiwara, H. Yagi, H. Akutsu, Y. Nosaka, Photoinduced changes of adsorbed water on a TiO₂ photocatalytic film as studied by ¹H NMR spectroscopy, *J. Phys. Chem. B* 107 (2003) 12042–12044.
- [60] J. Hu, C. Chen, Y. Zheng, G. Zhang, C. Guo, C.M. Li, Spatially separating redox centers on Z-scheme ZnIn₂S₄/BiVO₄ hierarchical heterostructure for highly efficient photocatalytic hydrogen evolution, *Small* 16 (2020), 2002988.
- [61] X. Li, Y. Sun, J. Xu, Y. Shao, J. Wu, X. Xu, Y. Pan, H. Ju, J. Zhu, Y. Xie, Selective visible-light-driven photocatalytic CO₂ reduction to CH₄ mediated by atomically thin CuIn₅S₈ layers, *Nat. Energy* 4 (2019) 690–699.
- [62] N. Uddin, Z. Sun, J. Langley, H. Lu, P. Cao, A. Wibowo, X. Yin, C.S. Tang, H. T. Nguyen, J.D. Evans, X. Li, X. Zhang, M. Heggen, R.E. Dunin-Borkowski, A.T. S. Wee, H. Zhao, N. Cox, Z. Yin, Ultrabroadband plasmon driving selective photoreforming of methanol under ambient conditions, *Proc. Natl. Acad. Sci. USA* 120 (2023), e2212075120.
- [63] Ž. Kovačić, B. Likozar, M. Huš, Photocatalytic CO₂ reduction: a review of ab initio mechanism, kinetics, and multiscale modeling simulations, *ACS Catal.* 10 (2020) 14984–15007.
- [64] J. Sheng, Y. He, J. Li, C. Yuan, H. Huang, S. Wang, Y. Sun, Z. Wang, F. Dong, Identification of halogen-associated active sites on bismuth-based perovskite quantum dots for efficient and selective CO₂-to-CO photoreduction, *ACS Nano* 14 (2020) 13103–13114.
- [65] S. Cheng, Z. Sun, K.H. Lim, T.Z.H. Gani, T. Zhang, Y. Wang, H. Yin, K. Liu, H. Guo, T. Du, L. Liu, G.K. Li, Z. Yin, S. Kawi, Emerging strategies for CO₂ photoreduction to CH₄: From experimental to data-driven design, *Adv. Energy Mater.* 12 (2022), 2200389.
- [66] J. Fu, J. Yu, C. Jiang, B. Cheng, g-C₃N₄-Based Heterostructured Photocatalysts, *Adv. Energy Mater.* 8 (2018), 1701503.
- [67] A. Agresti, A. Pazniak, S. Pescetelli, A. Di Vito, D. Rossi, A. Pecchia, M. Auf der Maur, A. Liedl, R. Larciprete, D.V. Kuznetsov, D. Saranin, A. Di Carlo, Titanium-carbide MXenes for work function and interface engineering in perovskite solar cells, *Nat. Mater.* 18 (2019) 1228–1234.
- [68] W. Wang, X. Bai, Q. Ci, L. Du, X. Ren, D.L. Phillips, Near-field drives long-lived shallow trapping of polymeric C₃N₄ for efficient photocatalytic hydrogen evolution, *Adv. Funct. Mater.* 31 (2021), 2103978.
- [69] Y. Gu, H. Feng, J. Zhao, M. Cui, Y. Li, Z. Li, Rational construction of edge-grafted g-C₃N₄ via cross-linking aromatic compounds with CF bonds for efficient photocatalytic H₂ evolution, *Chem. Eng. J.* 476 (2023), 146555.
- [70] X. Ma, L. Wang, Q. Zhang, H.-L. Jiang, Switching on the photocatalysis of metal-organic frameworks by engineering structural defects, *Angew. Chem. Int. Ed.* 58 (2019) 12175–12179.
- [71] T. Zhang, Z. Zhao, D. Zhang, X. Liu, P. Wang, Y. Li, S. Zhan, Superexchange-induced Pt-O-Ti³⁺ on single photocatalyst for efficient H₂ production with organics degradation in wastewater, *Proc. Natl. Acad. Sci. USA* 120 (2023), e2302873120.
- [72] Y.-J. Yuan, Z.-K. Shen, S. Song, J. Guan, L. Bao, L. Pei, Y. Su, S. Wu, W. Bai, Z.-T. Yu, Z. Ji, Z. Zou, Co-P bonds as atomic-level charge transfer channel to boost photocatalytic H₂ production of Co₂P/black phosphorus nanosheets photocatalyst, *ACS Catal.* 9 (2019) 7801–7807.